Ni_3S_2 nanostrips@FeNi-$NiFe_2O_4$ nanoparticles embedded in N-doped carbon microsphere: An improved electrocatalyst for oxygen evolution reaction

Li Xu[a], Sayyar Ali Shah [a,*], Habib Khan[c], Rani Sayyar[a], Xiaoping Shen[b], Iltaf Khan[d], Aihua Yuan[a,*], Waleed Yaseen[b], Zahid Ali Ghazi[e], Abdul Naeem[e], Habib Ullah[f] and Xiaohong Li[f]

[a]School of Environmental & Chemical Engineering Jiangsu University of Science and Technology Zhenjiang 212003, PR China

[b]School of Chemistry and Chemical Engineering Jiangsu University Zhenjiang 212013, PR China

[c]School of Physics, University of Electronic Science and Technology of China, Chengdu, 610054, PR China

[d]Beijing Academy of Safety Engineering and Technology, Beijing University of Aeronautics and Astronautics, Beijing 100191, China

[e]National Centre of Excellence in Physical Chemistry University of Peshawar , Peshawar. KPK, 25120, Pakistan

[f]Renewable Energy Group, College of Engineering, Mathematics and Physical Sciences, University of Exeter, Penryn Campus, Penryn, Cornwall TR10 9FE, United Kingdom

*Corresponding author. E-mail: sayyar786@gmail.com (S. A. Shah)

E-mail: aihua.yuan@just.edu.cn (A. H. Yuan)

Abstract

The designing and preparing of low-cost and easily available electrocatalyst for oxygen evolution reaction (OER) are crucial for many advanced energy technologies. Herein, the Ni_3S_2 nanostrips@FeNi-$NiFe_2O_4$ nanoparticles embedded in N-doped carbon (Ni_3S_2@FeNi-$NiFe_2O_4$/C) microspheres were synthesized as improved electrocatalyst for OER, using a facile heat-treatment method. The optimized Ni_3S_2@FeNi-$NiFe_2O_4$/C-3 sample exhibits enhanced electrocatalytic activity toward OER performance with an overpotential of 280 mV at 10 mA cm^{-2} and a small Tafel slope of 33.9 mV dec^{-1}. Furthermore, Ni_3S_2@FeNi-$NiFe_2O_4$/C-3 composite shows good stability in alkaline media. The outstanding electrocatalytic OER performance of composites was attributed due to the synergetic effect between Ni_3S_2 nanostrips and FeNi-$NiFe_2O_4$ nanoparticles and it is believed that the heterointerfaces between them act as active centers for OER. Additionally, N-doped carbon prevents the aggregation of Ni_3S_2@FeNi-$NiFe_2O_4$ species and enhances the conductivity of composites during the OER process.

Keywords: Oxygen evolution reaction, Ni_3S_2@FeNi-$NiFe_2O_4$ embedded in N-doped carbon, electrocatalyst, heat-treatment method, synergetic effect

1. Introduction

For depleting of fossil fuel and environmental issues, it is essential to develop advanced and more efficient clean energy technologies for the future [1]. Advanced technologies such as water splitting, metal-air batteries, and fuel cells have been broadly investigated and discussed for sustainable and clean energy sources [1-6]. Oxygen evolution reaction (OER) plays an important role in these advanced technologies. For example, OER occurs on the anode in water electrolysis in the electrolytic cell. However, OER involves multiple proton-coupled electrons transfer processes, and four protons couple with four electrons in a basic medium ($4OH^- \rightarrow 2H_2O+O_2 + 4e^-$). Therefore, OER displays sluggish kinetics and requires large overpotentials during water electrolysis. So, a highly active electrocatalyst is necessary to make the OER process more efficient. In this regard, the well-documented electrocatalysts are noble metal-based materials such as RuO_2 and IrO_2 [7,8]. However, low abundance on the earth and high costs reduced their application for large-scale manufacturing. Huge research attention has been paid to the designing and developing of highly active electrocatalysts for OER from non-precious metal elements [9-11].

Recently, the number of noble-metal free materials has been extensively investigated for water oxidation [12-15]. Among them, transition metals such as Fe, Co, and Ni elements have been attracted special attention due to their low cost and earth abundance [16-18]. Moreover, these transition elements are considered excellent electrocatalysts and display benchmark activities and stability for OER in alkaline conditions [16-18]. However, the single metallic-based materils often shows low catalytic activity for OER performance, as compared to bimetallic-based composites. Therefore, the catalytic activity of OER can be further enhanced by constructing heterostructure composites of the transition metals [19-22].

Nickel sulfides (Ni_3S_2) nanostructure materials are one of the promising electrocatalytic materials for OER because of their earth-abundance, high conductivity, and good redox chemistry [36-39]. Nevertheless, the intrinsic OER performance of Ni_3S_2 nanostructure is relatively low due to small active surface area, poor ion transport kinetics, and unsatisfactory stability [39]. To improve the OER performance of Ni_3S_2 nanostructure, various strategies have been reported to increase the number of accessible active sites as well as enhance the activity of Ni sites. The heazlewoodite mineral of Ni_3S_2 exist in nature, its nanostructure materials such as nanosheets [24], nanoneedles [39], nanowires [40], nanorods [41], and hollow microspheres [42], have been synthesized and displayed enhanced activity and good catalytic stability toward OER and water splitting. Although significant efforts are devoted to the morphology/size control of Ni_3S_2, the nanostrips type of Ni_3S_2 nanomaterials is yet to be investigated. On the other hand, metal ferrites are also promising candidates for OER due to their low cost, high electrochemical activity, high stability, and rich redox reversibility [43]. The OER performance of metal ferrites especially $NiFe_2O_3$ is rarely investigated, and there are only a few reports on the electrocatalytic OER activity of $NiFe_2O_3$. Mahala *et. al.* reported $NiFe_2O_3$ nanosheets and nanobipyramids which required overpotentials of 1.69 and 1.77 V *vs*. RHE at a current density of 10 mA cm^{-2}, respectively [43]. Yang *et. al*. reported a series of atomically thin $NiFe_2O_4$ quantum dots for enhanced OER performance [44]. Recently, Choi and co-workers prepared $NiFe_2O_{4-x}$ nanoparticles/$NiMoO_4$ nanowires composite to construct an extended interface with strong electronic interactions that demonstrated an overpotential of 326 mV at a current density of 600 mA cm^{-2} and good stability [45]. These reports demonstrate that heterostructure Ni_3S_2 and $NiFe_2O_3$ composites can be an effective catalyst for OER.

It is believed that both cation and anions positively influence catalytic performance [27-30]. For the active centers of Ni-Fe composites, different opinions are reported in the literature. Some authors suggested that the active center for oxygen evolution is Ni, the Fe induces a partial charge transfer effect to enrich the electronic structure of Ni sites [31,32], while others believed, Fe to be catalytically active sites with optimal adsorption energies for the intermediates during the catalytic OER process[33] and Ni provides conductive support [34,35]. No matter which metal center be the active site, it is widely accepted that composites materials show enhanced OER performance than single-phase structure. Anion also plays an important role, and it can alter the electronic structure of the metal's active sites and improve the OER performance of the active center [29,30]. Considering these reports in mind, we were inspired to design and synthesize a new heterostructure composite, composed of Ni_3S_2 and $NiFe_2O_3$ nanomaterials via facile strategy for the enhanced OER performance.

In this study, we reported Ni_3S_2 nanostrips@FeNi-$NiFe_2O_4$ nanoparticles embedded in N-doped carbon microsphere (Ni_3S_2@FeNi-$NiFe_2O_4$/C) catalysts for OER. The Ni_3S_2@FeNi-$NiFe_2O_4$/C composites were prepared by a facile one-step heat-treatment process using urea, Ni, and Fe compounds as precursors. The obtained Ni_3S_2@FeNi-$NiFe_2O_4$/C hybrids exhibit enhanced electrocatalytic activity toward OER performance. The optimized Ni_3S_2@FeNi-$NiFe_2O_4$/C-3 sample displays outstanding OER performance with an overpotential of 280 mV at a current density of 10 mA cm^{-2} and a small Tafel slope of 33.9 mV dec^{-1}. The composite also shows good stability in a 1 M alkaline solution.

2. Experimental section

2.1 Materials and chemicals

$NiCl_2 \cdot 6H2O$ (≥99 %) was purchased from Shanghai McLean Biochemical Technology Co., Ltd. $Fe_2SO_4 \cdot 7H_2O$ (≥99 %) was purchased from Sinopharm Chemical Reagent Co., Ltd. Urea (99 %) and absolute ethanol was purchased from Jiangsu Qiangsheng Functional Chemical Co., Ltd. Nafion solution was purchased from Alfa Aesar. The deionized water was used for all of our experiments.

2.2 Synthesis of Ni_3S_2@FeNi-$NiFe_2O_4$/C composites

The Ni_3S_2@FeNi-$NiFe_2O_4$/C composites were synthesized by a facile one-step heat-treatment process using urea, Ni, and Fe precursors. The urea (1 g), $NiCl_2 \cdot 6H_2O$ (0.2 g), and $FeSO_4 \cdot 7H_2O$ (0.25 g) were added simultaneously into ethanol. The mixture was stirred for 30 min and kept in a vacuum oven at room temperature to evaporate the solvent. Then, the obtained mixture was heated at 750 ºC for 1 h under the nitrogen atmosphere. The heating rate was 2 ºC min^{-1}. The products were collected, when cooled to room temperature naturally. It was washed with water and ethanol, followed by drying in a vacuum oven at 50 ºC.

The other samples were also prepared with the same procedure, and the initial precursor composition of the reaction mixture for these samples is given in Table S1 (supporting information).

2.3 Synthesis of Ni-NiO/C and Fe_3O_4/C product

The Ni-NiO/C-7 and Fe_3O_4/C-8 are also prepared with the above procedure. In the case of Ni-NiO/C-7 product, only urea and $NiCl_2 \cdot 6H_2O$ (0.2 g) were used as reaction mixture, while for Fe_3O_4/C-8, urea and $FeSO_4 \cdot 7H_2O$ (0.25 g) were taken as initial precursors (Table S1).

2.4 Material characterizations

The microstructure of surfaces of the prepared products was studied by scanning electron microscopy (SEM, XL30-FEG). Transmission electron microscopy (TEM, JEM-2100F, JEOL)

characterization was applied to further observe the morphology and structure of the product. The crystalline structure of materials was analyzed from X-ray diffraction (Bruker SMART APEX2) analysis. The thermogravimetric analysis (TGA) was obtained from a thermal analyzer (NETZSCH STA 449F3). Raman spectrum was acquired using Raman Microscope (JYHR800). Metals contents in samples were obtained using an inductively coupled plasma optical emission spectrometer (ICP-OES. PerkinElmer Avio™ 200). Brunauer-Emmett-Teller (BET) surface area was obtained from the specific surface porosity analyzer (ASAP2020 Mack instruments). The analysis of the chemical composition of products was studied using X-ray photoelectron spectroscopy (XPS, AXIS ULTRA).

2.5 Electrochemical measurements

All electrochemical tests were carried out using a three-electrode cell on an electrochemical workstation. A glassy carbon, graphitic carbon rod (dimension: diameter and length are 7 mm and 5 cm, respectively), and Hg/HgO electrode were used as working, counter, and reference electrodes, respectively. The homogeneous ink for the working electrode was prepared by dispersing 4 mg of catalyst and 30 μL of Nafion solution (5 wt %) in 970 μL of ethanol and sonicated for 30 min. Then, 5 μL drop of ink was put on a glassy carbon electrode and electrochemical tests were performed after dried in air. Before linear sweep voltammetry (LSV), cyclic voltammograms (CVs) were performed between 0 and 0.7 V versus Hg/HgO in 1 M KOH aqueous solution at a scan rate of 100 mV s^{-1} for 50 cycles. The LSV was measured at a scan rate of 5 mV. The double-layer capacitance (C_{dl}) values were calculated from the CV curves with a potential window of 0 to 0.1 V *vs.* Hg/HgO at different scan rates. Electrochemical impedance spectroscopy (EIS) measurements were carried out in the frequency range of 100 kHz to 100 mHz

of an AC voltage of 5 mV in 1 M KOH solution. The potential is expressed to those *vs*. a reversible hydrogen electrode (RHE).

The turnover frequency (TOF) values were calculated assuming that all Ni or Fe ions in the composites are active and participating in the OER catalytic reaction. The TOF values were calculated as follows.

TOF = jS/4Fn

Where j is the measured current density (mA cm^{-2}) at η= 0.35 V; S represents the surface area of glassy carbon electrode (0.0707 cm^2); 4 is the number of electrons per O_2 molecular. F (96485.3 C mol^{-1}) is Faraday constant; n is the moles of Ni or Fe ions in samples and calculated from the loading amount of catalyst on the working electrode.

3. Results and discussion

3.1 Fabrication and characterization

The Ni_3S_2@FeNi-$NiFe_2O_4$/C composites were prepared by a simple one-step strategy as shown in Scheme 1. The $NiCl_2$ and $FeSO_4$ salts were dissolved into the respective Ni^{2+}, Cl^{2-}, $Fe^{2+,}$ and SO_4^{2-} ions in ethanol. At the same time, the urea molecules were also dissolved in the aqueous solution. The anion and cation of these salts interact with urea. After evaporation of the solvent, the homogenous mixture of the anion, cation, and urea molecules is formed. During the heat treatment, some Ni species reacted with sulfate ions and formed Ni_3S_2 nanostrips. Fe and the remaining Ni ions were converted to FeNi alloy. The FeNi alloy partially oxides particularly on the surface to form FeNi-$NiFe_2O_4$. Meanwhile, urea was converted into N-doped carbon and the residue gases generated during the process were released with carries gas. As a result, the Ni_3S_2@FeNi-

$NiFe_2O_4$/C composite was formed as a final product. For the different compositions of Ni_3S_2@FeNi-$NiFe_2O_4$/C composites and details of the synthesis process, (Experimental Section).

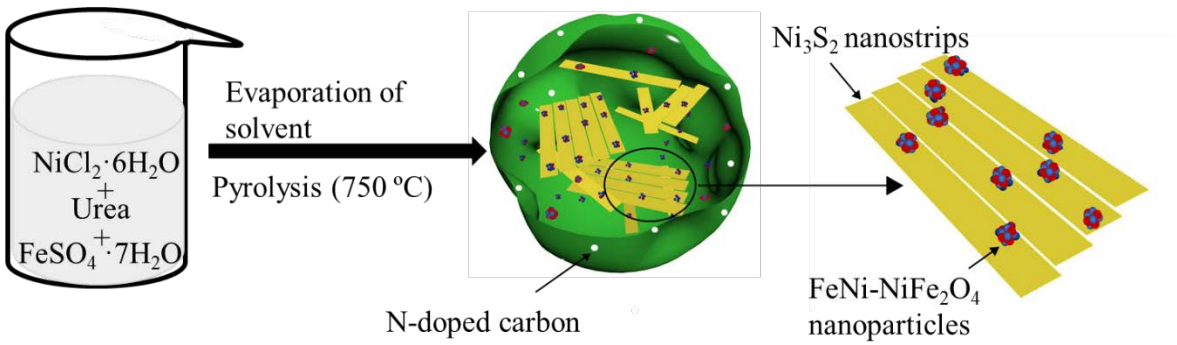

Scheme 1. Illustration of the synthesis process of Ni_3S_2@FeNi-$NiFe_2O_4$/C composites.

The crystal structures of as-prepared Ni_3S_2@FeNi-$NiFe_2O_4$/C, Ni-NiO/C-7, and Fe_3O_4/C-8 samples were characterized and analyzed using XRD technique as shown in Fig. 1. The diffraction peaks of the Ni_3S_2@FeNi-$NiFe_2O_4$/C composites would be indexed as a mixture of Ni_3S_2, FeNi, and $NiFe_2O_3$. The peak at about 21.7º, 30.9º, 37.7º,38.2º, 49.6º,49.9º, 54.6º, 54.9º, 55.1º, and 55.3º can match well with (101), (110) (003), (021), (113), (211), (104), (122), and (300) crystalline planes of heazlewoodite Ni_3S_2 (JCPDS card No. 44-1418), respectively. The diffraction peak at about 44.1º, 51.4º, 75.8º can be associated (111), (200), (220) of FeNi alloy (JCPDS card No. 38-0419) and those at 30º, 35.5º 56.8º, 62.5º can be attributed 220º, 311º, 511º, 440º of $NiFe_2O_4$ (JCPDS card No. 54-0964), respectively. The intensity of Ni_3S_2 phase gradually increases from Ni_3S_2@FeNi-$NiFe_2O_4$/C-1 to Ni_3S_2@FeNi-$NiFe_2O_4$/C-3 and then decreases up to Ni_3S_2@FeNi-$NiFe_2O_4$/C-6 composites. The strong intensities of Ni_3S_2 peaks in Ni_3S_2@FeNi-$NiFe_2O_4$/C-3 sample indicate the presence high amount of Ni_3S_2 phase. When only $NiCl_2$ precursor and urea were used in the same experimental conditions, the peaks at 44.5º, 51.8º, 76.3º are observed, which

are consistent with (111), (200), and (220) lattice plane of the metallic cubic Ni (JCPDS card No. 04-0850), respectively. On the other hand, when $FeSO_4$ was treated with urea, the peaks at 30º, 35.2º, 37º, 43.9º, 53.2º, 56.7º, and 62.4º are observed, which are related to (220), (311), (222), (400), (422), (511), (440) lattice planes of magnetite Fe_3O_4 (JCPDS card No. 19-0629), respectively. The very small peak shown by the asterisk is due to metallic Fe. No obvious diffraction peaks of carbon are observed in XRD patterns. This is possibly due to their relatively low diffraction intensity.

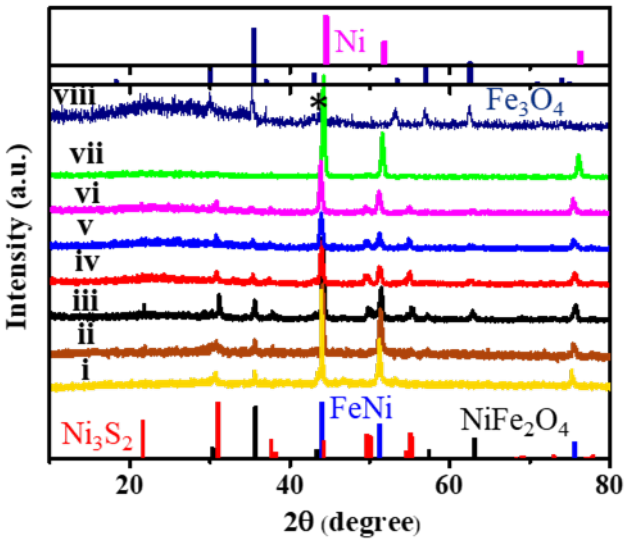

Fig. 1. XRD patterns of the as-prepared samples. (i) Ni_3S_2@FeNi-$NiFe_2O_4$/C-1, (ii) Ni_3S_2@FeNi-$NiFe_2O_4$/C-2, (iii) Ni_3S_2@FeNi-$NiFe_2O_4$/C-3, (iv) Ni_3S_2@FeNi-$NiFe_2O_4$/C-4, (v) Ni_3S_2@FeNi-$NiFe_2O_4$/C-5, (vi) Ni_3S_2@FeNi-$NiFe_2O_4$/C-6, (vii) Ni-NiO/C-7, (viii) Fe_3O_4/NC-8. The standard patterns of Ni_3S_2 (JCPDS No. 44-1418), $NiFe_2O_4$ (JCPDS No. 54-0964), FeNi (JCPDS No. 38-0419), Ni (JCPDS No. 04-0850), Fe_3O_4 (JCPDS No. 19-0629) are also shown for references. The weak peak denoted with an asterisk (*) is possibly attributed due to metallic Fe.

The morphology and microstructure of the composite were observed from the SEM and TEM characterizations. Analysis of SEM images shows that the Ni_3S_2@FeNi-$NiFe_2O_4$/C-3 composite

is composed of a microsphere-like structure with irregular shapes (Fig. 2a). The sizes of these microsphere-like structures are from sub-micrometer to a few micrometers. Careful observation indicates that surfaces of most microspheres are wrinkles (Fig. 2b). The morphology of FeNi-Ni_3S_2@FeNi-$NiFe_2O_4$/C-1 (Fig. S1a,b) and Ni_3S_2@FeNi-$NiFe_2O_4$/C-2 (Fig. S1c,d) FeNi-Ni_3S_2@FeNi-$NiFe_2O_4$/C-4 (Fig. S1e,f) and Ni_3S_2@FeNi-$NiFe_2O_4$/C-5 (Fig. S1g,h) samples are very similar to that of Ni_3S_2@FeNi-$NiFe_2O_4$/C-3, while the Ni_3S_2@FeNi-$NiFe_2O_4$/C-4 sample some small particles can also be seen (Fig. S1i,j). On the other hand, the Ni-NiO/C-7 (Fig. S1k,l) and Fe_2O_4/C-6 (Fig. S1m,n) samples more particles can be seen. This may be due to Ni and Fe precursors, which are mostly converted to Ni-NiO and Fe_3O_4 particles embedded in carbon during heat treatment. The particles observed in the Ni_3S_2@FeNi-$NiFe_2O_4$/C-6 sample are also due to the low amount of Fe precursors in the reaction mixture.

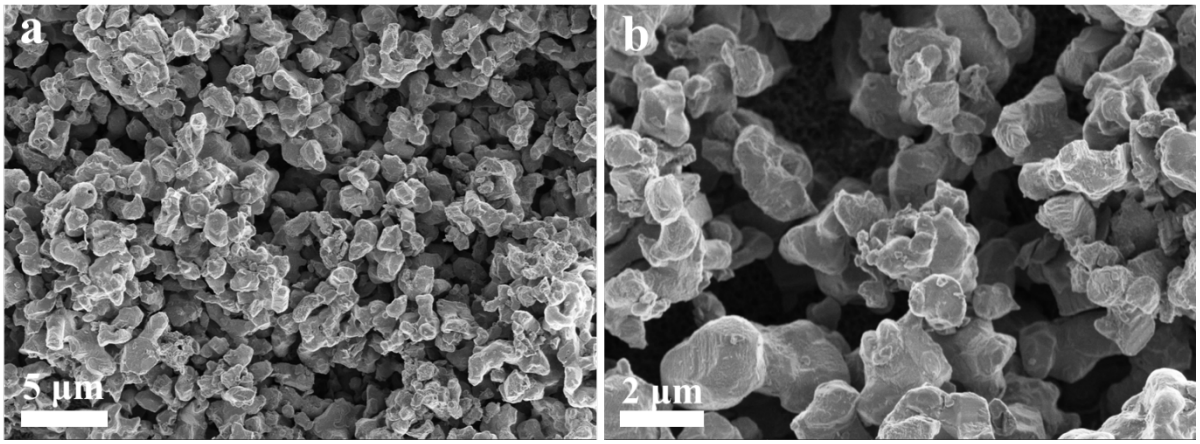

Fig. 2. SEM images of Ni_3S_2@FeNi-$NiFe_2O_4$/C-3 catalyst at (a) low, and (b) high magnification.

The TEM and elemental mapping images of the Ni_3S_2@FeNi-$NiFe_2O_4$/C-3 composite are shown in Fig. 3. The observation of TEM image also confirms that Ni_3S_2@FeNi-$NiFe_2O_4$/C-3 composite has a microsphere-like structure with a wrinkle periphery (Fig. 3a). The rectangular flaky structure can be seen in the microsphere (Fig. 3b). The microspheres are high transparency in those places,

where no flaky structures are observed. The wrinkle periphery and transference places may be mostly N-doped carbon. The rectangular flaky structures were further magnified (Fig. 3c). Actually, these rectangular flaky structures consist of nanostrips and several nanostrips in flakes from single to few nanostrips. The areas of these nanostrips are ranging from hundreds of square nanometers to several square micrometers. Some nanoparticles can be seen on the surface of nanostrips (Fig. 3d). These nanoparticles are most possibly due to the FeNi-$NiFe_2O_4$ particles. The high-resolution TEM (HRTEM) images show carbon consisting of both layers and amorphous structures (Fig. S2a). The interlayer spacing of carbon is about 0.38 nm, indicating the graphitization of carbon (Fig. S2b). Raman spectrum of the Ni_3S_2@FeNi-$NiFe_2O4$/C-3 sample also shows a well-defined D and G at 1365 and 1586 cm^{-1}, which is the characteristic of carbon materials (Fig. S3). The I_D/I_G ratio is 1.9 which indicates the presence of graphitic carbon in the composite. The HRTEM images of typical nanostrips and nanoparticles clearly display lattice fringes and well-defined interfaces (Fig. 3e-g). The lattice fringes with a spacing of about 0.208 nm are consistent with the (111) lattice plane of FeNi alloy and spacing of about 0.25 nm on the surfaces of FeNi alloy consistent (311) lattice plane of $NiFe_2O_4$ (Fig. 3e). The lattice fringes with spacing 0.24 nm are matched with (021) of Ni_3S_2 and lattice fringes with spacing 0.28 of (110) lattice plane indicate the layer of Ni_3S_2. The (111) crystal planes of FeNi alloy with a lattice spacing of 0.208 nm on surface (211) crystal planes of Ni_3S_2 can also be observed (Fig. 3g). The well-defined interfaces between Ni_3S_2 nano strip and FeNi-$NiFe_2S_3$ nanoparticles can boost the OER performance due to synergistic effects.

Elemental distributions of the composite were scanned by EDS measurement attached with TEM. Fig. 3h shows the dark field images of the product. The elementary mapping images of Ni, S, Fe, C, N, and O are shown in Fig. 3i-n, respectively. The Ni and S show homogenous

distributions in the composites suggesting that these flakes are composed of Ni and S. The dense and light signals of the Fe elements indicate the presence of Fe in nanoparticles. It can be seen that carbon signals are more obvious at the edges of the microsphere and N content is weaker, suggesting N-doped carbon enveloped the Ni_3S_2@FeNi-$NiFe_2O_4$ species.

The Ni and Fe contents in the as-prepared samples were determined by inductively coupled plasma as listed in Table S2. The Fe content in the composites sequentially decreases from sample Ni_3S_2@FeNi-$NiFe_2O_4$/C-1 to Ni_3S_2@FeNi-$NiFe_2O_4$/C-6. The weight loss of Ni_3S_2@FeNi-$NiFe_2O_4$/C-3 composite was determined by TGA as shown in Fig. S4a. The weight loss is about 6 % below 300 ºC, which may be ascribed to the loss of adsorbed water. On further heating, no weight loss occurred which confirms the thermal stability of the composites. However, surfaces of the composite are oxidized after synthesis. The weight loss (7 %) can be seen after 600 ºC, which may be due to the oxidation of carbon and sulfur, to CO_2 and SO_2 species, respectively. The total weight loss of Ni_3S_2@FeNi-$NiFe_2O_4$/C-3 composite up to 700 ºC is about 13 %, indicating the good stability of composites. The specific surface area of the Ni_3S_2@FeNi-$NiFe_2O4$/C-3 sample is 13.2 m^2 g^{-1}, measured by the BET analyses (Fig. S4b).

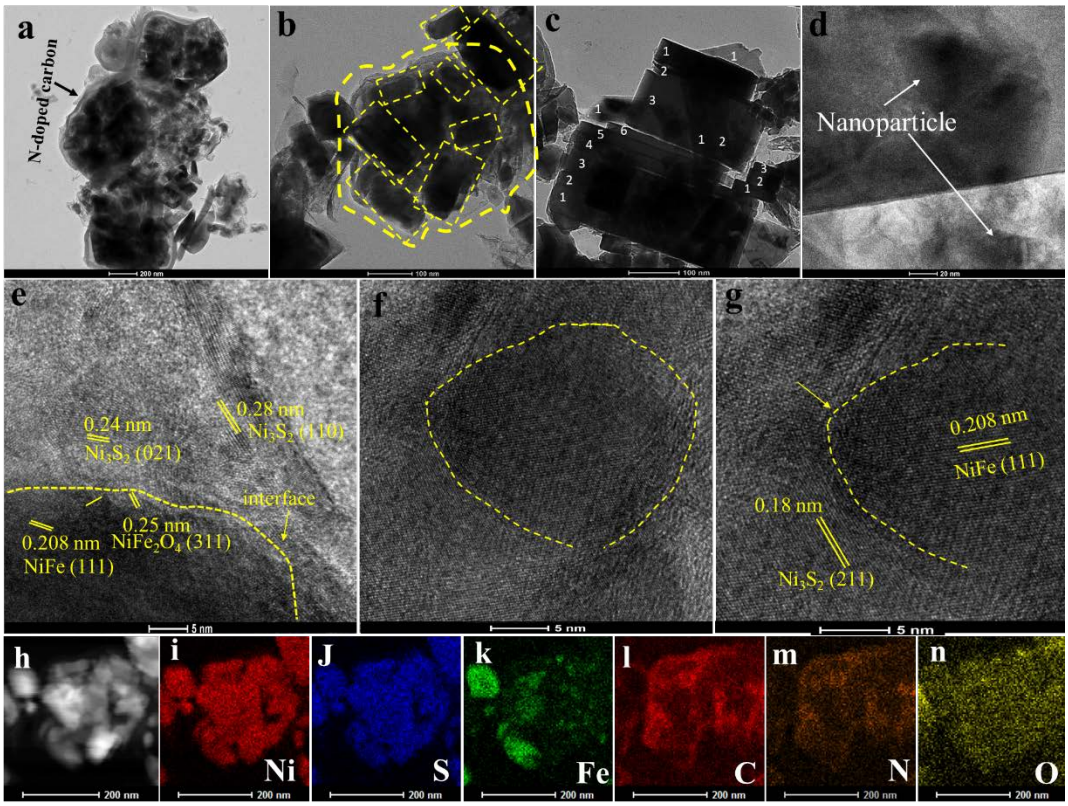

Fig. 3. (**a-d)** TEM and (e-g) HRTEM images of the Ni_3S_2@FeNi-$NiFe_2O_4$/C-3 sample. (h) Dark-field TEM image and (i-n) element mapping images of Ni_3S_2@FeNi-$NiFe_2O_4$/C-3 catalyst.

The XPS analysis was performed to determine the valance states and elemental composition of the sample. The survey XPS spectrum of Ni_3S_2@FeNi-$NiFe_2O_4$/C-3 displays peaks for Ni, Fe, C, S, N, and O elements and for comparison, the survey XPS spectra of Ni-NiO/C-7 and Fe_3O_4/C-8 are also shown in Fig. S5a. The XPS spectrum of Ni 2p region of Ni_3S_2@FeNi-$NiFe_2O_4$/C-3 can be deconvoluted into different peaks (Fig. 4a). The relatively weak peak at around 853 and 872 eV can be associated with zero valance Ni of FeNi alloy and/or Ni_3S_2 strips [24,46,47]. The peaks centered at 873.7 and 855.9 eV can be related to Ni $2p_{3/2}$ and Ni $2p_{1/2}$, of Ni^{2+} valance state, respectively [47]. A pair of peaks at around 861.6 and 879.4 eV are ascribed to the satellite peaks of Ni [47]. The peaks Ni $2p_{3/2}$ and Ni $2p_{1/2}$ of Ni^{2+} of NiFe-$NiFe_2O_4$@Ni_3S_2/C-3 composite are

shifted to slightly higher binding energy compared to Ni-NiO/C-7 sample. The blue-shifts indicate electron transfer between Ni and Fe species in NiFe-$NiFe_2O_4$@Ni_3S_2/C-3 composite, which promotes Ni to high oxidation states [48]. Previously, it is suggested that the high oxidation states of metals can promote OER performances [49]. The Fe 2p can be deconvoluted into different valance states and the satellite peaks (Fig. 4b). The small peak at 707.6 eV is due to metallic Fe of zero valance states [40]. The peaks at around 710.8 and 713.6 eV of Fe $2p_{3/2}$ band indicate the presence of both Fe^{2+} and Fe^{3+} oxidation states of Fe, respectively [50,51]. Similarly, peaks at 723.8 and 226.1 eV of Fe $2p_{1/2}$ bands are also characteristic of Fe^{2+} and Fe^{3+} oxidation states of Fe, respectively [50,51]. The broad spectra of Fe^{2+} and Fe^{3+} oxidation states of Fe $2p_{3/2}$ band in the NiFe-$NiFe_2O_4$@Ni_3S_2/C-3 sample compared to Fe_3O_4/C-8 product is possibly due to interaction between Ni and Fe species. The XPS spectrum of S 2p region is shown in Fig. 4c and can be deconvoluted into different peaks. The bands' peaks around at 162 and 163.3 eV are associated with binding energy S $2p_{3/2}$ and S $2p_{1/2}$, respectively and suggesting the presence of metal sulfides [24]. The peak at high binding energy at 168.7 eV is related to sulfate species and possibly due to the oxidation of sulfur species in the air [24]. The XPS spectrum of C 1s region displays an obvious peak at 284.4 eV and can be related to the characteristic peak of carbon materials of C=C/C–C bonds (Fig. 4d) [46,52,53]. The other peaks at 285.9 and 288.8 eV can be associated with carbon bonded the C-N/C–O and C=O bonding species, respectively [46,52,53]. The XPS spectrum of N Is, the peaks at 398.7, 399.9 and 401.1 eV can be attributed to pyridinic, pyrrolic, and graphitic nitrogen respectively (Fig. S5b) [46,52,53]. The high-resolution spectrum for the O 1s region is shown in Fig. S5c. The peak at around 529.9 eV can be related to Metal-O bonds [48]. The peaks at 531.4 and 532.8 eV are related to C-O/C=O bonds and physic/chemisorbed water, respectively [48].

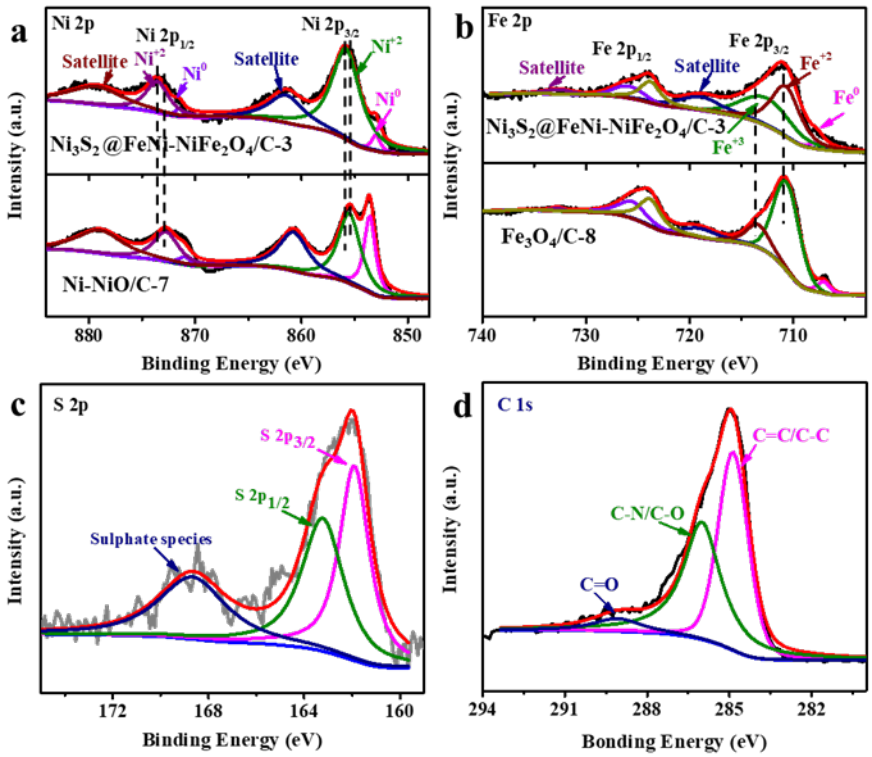

Fig. 4. High-resolution XPS spectra, (a) Ni 2p region of NiFe-$NiFe_2O_4$/Ni_3S_2/C-3 and Ni-NiO/C-7 samples, and (b) Fe 2p region of NiFe-$NiFe_2O_4$/Ni_3S_2/C-3 and Fe_3O_4/C-8 samples. High-resolution XPS spectra (c) S 2p region, and (d) C 1s region of NiFe-$NiFe_2O_4$/Ni_3S_2/C-3 sample.

3.2 Electrocatalytic OER performance

The as-prepared samples and IrO_2 catalyst are used as electrocatalysts for OER performance. The OER activities of the sample were measured by a three-electrode set up in a 1M KOH aqueous solution. Fig. 5a shows the LSV carves of as-prepared samples and IrO_2 catalyst. Generally, the OER performance of the catalyst is estimated from the overpotential value at a current density of 10 mA cm^{-2}, which is considered a metric relevant to solar fuel synthesis. The Ni_3S_2@FeNi-$NiFe_2O_4$/C-3 sample exhibits the best OER performance with an overpotential 280 mV at the current density 10 mA cm^{-2}, which is better than that of IrO_2 catalyst. The LSV carve of Ni-NiO/C-7 and Fe_3O_4/C-8 sample reveals the lower catalytic activity for OER performance and requires an

overpotential of 567 and 617 mA at the current density 10 mA cm^{-2}, respectively. The Ni_3S_2@FeNi-$NiFe_2O_4$/C-1 (378 mV), Ni_3S_2@FeNi-$NiFe_2O_4$/C-2 (296 mV), Ni_3S_2@FeNi-$NiFe_2O_4$/C-4 (390 mV), Ni_3S_2@FeNi-$NiFe_2O_4$/C-5 (410 mV), and Ni_3S_2@FeNi-$NiFe_2O_4$/C-6 (456 mV) composites also displayed better OER performance at current density 10 mA cm^{-2} than those of Ni-NiO/C-7 and Fe_3O_4/C-8 catalysts (Fig. 5b). In the case of as-prepared samples, the overpotential at current density 10 mA cm^{-2} of Ni_3S_2@FeNi-$NiFe_2O_4$/C composites, firstly, increases and then decreases by adding more $FeSO_4$ precursor to the reaction mixture, and optimal sample of Ni_3S_2@FeNi-$NiFe_2O_4$/C-3 is observed for the OER performance. This suggests that optimal ratio Ni_3S_2 nanostrips and FeNi-$NiFe_2O_4$ nanoparticles are in Ni_3S_2@FeNi-$NiFe_2O_4$/C-3 sample and formed heterointerfaces as catalytic active sites for outstanding OER performance. This clearly indicates that the enhanced catalytic activity can be ascribed to the synergistic effect between Ni_3S_2 nanostrips and FeNi-$NiFe_2O_4$ nanoparticles.

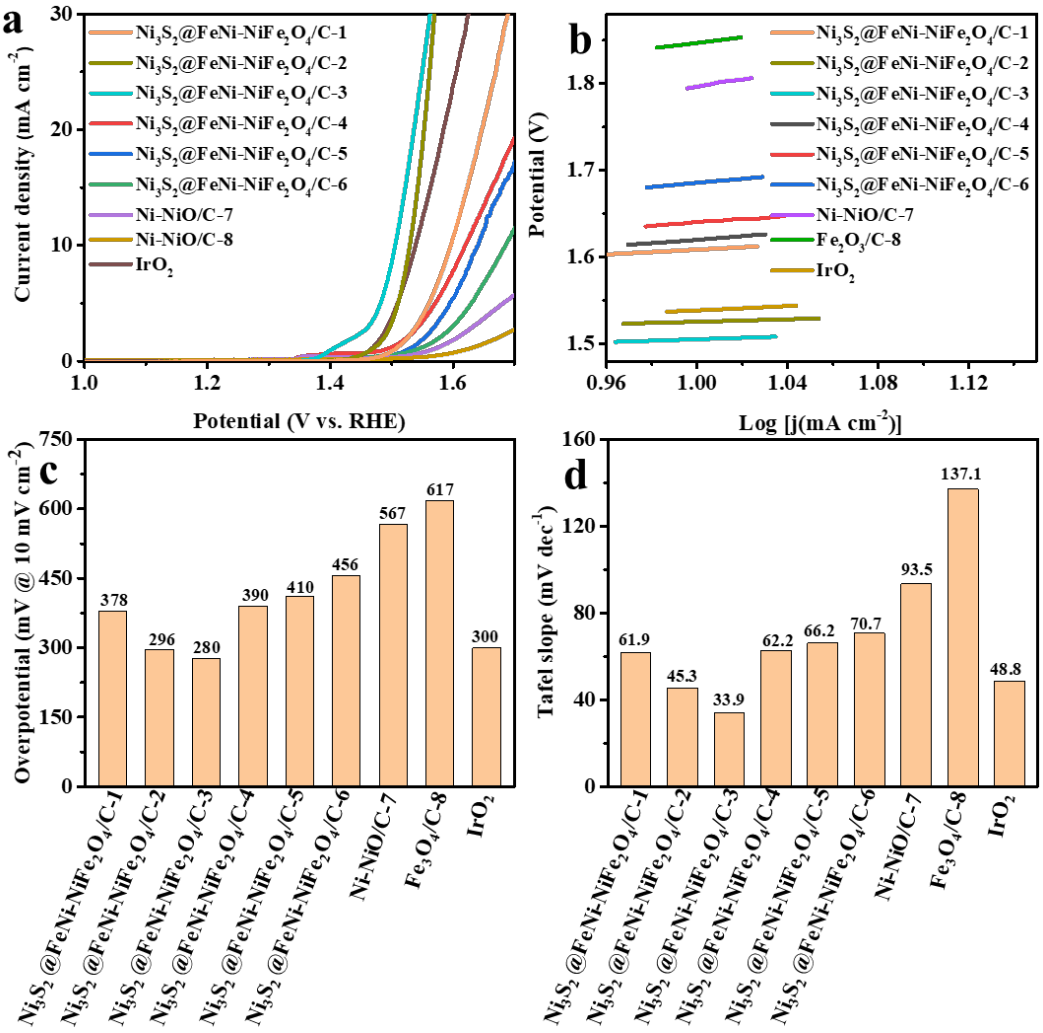

Fig. 5. (a) LSV curves and (b) comparison of overpotentials for a current density of 10 mA cm^{-2} of the as-prepared samples and IrO_2 catalyst. (c) The corresponding Tafel slopes are obtained from LSV curves of "a". (d) comparison of Tafel slopes of as-prepared samples and IrO_2 catalyst.

To further understand the performance of electrocatalysts, Tafel plots are calculated from the LSVs curves (Fig. 5c). The Tafel slope is obtained by fitting linear portions of LSV curves into the Tafel equation. The Tafel slope of the Ni_3S_2@FeNi-$NiFe_2O_4$/C-3 composite is 33.9 mV dec^{-1} which is smaller than those of IrO_2 (48.8 mV dec^{-1}), Ni_3S_2@FeNi-$NiFe_2O_4$/C-1 (61.9 mV dec^{-1}),

Ni_3S_2@FeNi-$NiFe_2O_4$/C-2 (45.3 mV dec^{-1}), Ni_3S_2@FeNi-$NiFe_2O_4$/C-4 (62.2 mV dec^{-1}), Ni_3S_2@FeNi-$NiFe_2O_4$/C-5 (66.2 mV dec^{-1}), Ni_3S_2@FeNi-$NiFe_2O_4$/C-6 (70.7 mV dec^{-1}), Ni-NiO/C-7 (93.5 mV dec^{-1}), and Fe_3O_4/C-8 (137.1 mV dec^{-1}) (Fig. 5d). Comparative analysis of the above results and discussion led us to conclude that Ni_3S_2@FeNi-$NiFe_2O_4$/C-3 composite has favorable reaction kinetics and thus shows better OER performance. While the relatively high Tafel slope value of other samples indicates the slow reaction kinetics. The Ni_3S_2@FeNi-$NiFe_2O_4$/C-3 sample shows comparable or better catalytic activity than those of $NiFe_2O_4$ and Ni_3S_2 based materials (Table S3) such as $NiFe_2O_4$ nanosheets (η_{10}= 1.69 V vs. RHE) [43], $NiFe_2O_4$ quantum dot (η_{10}= 262 mV) [44], Ni-Ni_3S_2 nanoparticles encapsulated in N-doped carbon matrix (η_{10}= 284.7 mV) [54], BG@Ni/ Ni_3S_2 (η_{100} = 320 mV) [55], and Ni_3S_2@C (η_{100} = 298 mV)[56] are reported on glassy carbon electrode.

It is observed that oxygen evolution occurs at high overpotential in low concentration alkaline solution and more facile in strongly alkaline solution. However, oxygen evolution is equally important in both low and high concentration solutions from viewpoint of devices. For example, oxygen evolution is commonly performed in a 0.1 M KOH solution in a metal−air battery [57], while water splitting is usually performed in a high concentration alkaline solution [58]. We also performed the OER catalytic activity of the best sample in 0.1 and 6 M KOH solution. The overpotential of the Ni_3S_2@FeNi-$NiFe_2O_4$/C-3 composite sample is 360 and 232 mV at a current density of 10 mA cm^{-2} in 0.1 and 6 M KOH solution, respectively (Fig. S6a). The Tafel slope of the Ni_3S_2@FeNi-$NiFe_2O_4$/C-3 composite is 90 and 30.1 mV dec^{-1} in 0.1 and 6 M KOH solution (Fig. S6b), respectively. Interestingly, Ni_3S_2@FeNi-$NiFe_2O_4$/C-3 composite displays better OER performance in 0.1 M KOH solution than those of Ni-NiO/C-7 and Fe_3O_4/C-8 catalysts in 1 M KOH solution. It also shows superior OER compared to transition-metal-based composites, such

as Co_3O_4/porous carbon (η_{10}= 360 mV) [59], $FeCoO_x$ (η_{10} = 400 mV) [60], cobalt carbonate hydroxide/C (η_{10} = 470 mV) [61], and MOF-derived $Ni^{II}Fe^{III}$@NC (η_{10} = 360 mV) [62], and $Ni^{II}Fe^{II}$@NC catalyst (η_{10} = 394 mV) [62].

The improved catalytic activity of the catalyst is mainly due to increased numbers of active sites on its surface area or enhanced intrinsic activity of each active site. To reveal the high catalytic activity of as-prepared samples, the electrochemical surface area (ECSA) of these products was investigated by measuring the double-layer capacitance (C_{dl}). The CV curves of the as-prepared catalysts are shown in Fig. S7a-h. The C_{dl} value is in a positive relationship with ECSA and thus is usually used to describe the ECSA. The C_{dl} value of Fe_3O_4/C-8 and Ni-NiO/C-7 are 0.033 and 0.052 mF cm^{-2}, respectively (Fig. 6a), indicating the smaller number of active sites. The C_{dl} values of the composite catalysts are 0.12. 0.16, 0.35, 0.10, 0.099, and 0.058 mF cm^{-2} for NiFe-$NiFe_2O_4$@Ni_3S_2/C-1, NiFe-$NiFe_2O_4$@Ni_3S_2/C-2, NiFe-$NiFe_2O_4$@Ni_3S_2/C-3, NiFe-$NiFe_2O_4$@Ni_3S_2/C-4, NiFe-$NiFe_2O_4$@Ni_3S_2/C-5, and NiFe-$NiFe_2O_4$@Ni_3S_2/C-6, respectively. The C_{dl} of $NiFe_2O_4$@Ni_3S_2/C-3 sample is 6.7 and 10.6 times higher than those of Ni-NiO/C-7 and Fe_3O_4/C-8, respectively, and also higher than other prepared composites. The increase in C_{dl} values NiFe-$NiFe_2O_4$@Ni_3S_2/C composites clearly indicates the presence of heterointerfaces, which act as active catalytic sites for OER performance. The Fe and Ni contents were measured in the as-prepared composites to normalize the catalytic active sites. The TOF values of Ni (TOF_{Ni}) and Fe (TOF_{Fe}) were calculated (Table S4). It is observed that the TOF_{Ni} and TOF_{Fe} values of the optimized NiFe-$NiFe_2O_4$@Ni_3S_2/C-3 samples are 0.0418 and 0.0484 s^{-1}, respectively. These observations suggest large numbers of heterointerfaces that enhance the activity of each catalytic site and consequently improve the OER catalytic performance.

The OER performance of Ni-NiO/C-7 and Fe_3O_4/C-8 samples alone are very poor, while NiFe-$NiFe_2O_4$@Ni_3S_2/C composites show an enhanced catalytic activity toward OER. The metal-based compounds, where metal is an active center for the OER in basic solution. The OER process proceeds through various intermediates including M–OH, M=O, and M–O–OH (M = metal active center) at active centers [63,64]. To release oxygen molecules in bimetallic composites, both single and dual-site mechanisms have been proposed [64,65]. In the single-site mechanism, it is proposed that nucleophilic attack of OH^- on M=O results in the formation of O–O bond [64,66], while in the dual-site mechanism, the formation O–O bond arises from M–O–O–M′ linkage [66-68]. For NiFe heterojunction composites, Ni site is believed to act active centers and induces OER process by high valent Ni=O or NiOOH intermediate and Fe enhances the oxidation of near Ni sites. On the other hand, Fe has been suggested as the active site and Ni is only a synergistic agent that acts as conductive support.

In the case of NiFe-$NiFe_2O_4$@Ni_3S_2/C-3 catalyst, the strong coupling between Ni_3S_2 nanostrips and NiFe-$NiFe_2O_4$ particles facilitates and forms heterointerfaces. The strong electronic interactions at the interfaces play an important role in the improved OER performance. The XPS results show the electronic interactions and electron transfer process between Fe and Ni in the composite of NiFe-$NiFe_2O_4$ and Ni_3S_2 species. The transfer of electrons occurs from Ni to Fe sites and induces the Ni to high oxidation states. This modifies the electronic structure of metal sites at heterointerfaces. On the other hand, the anion also affects the electronic structure of metal sites. The anion in the Ni_3S_2 species is an S element while that of NiFe-$NiFe_2O_4$ is an O element. Most active centers may be located on the heterointerfaces. Assuming these factors, the OER process follows the dual site's mechanism (Fig. S8).

The metals sites are under coordinated and bonded to OH^- ions in the alkaline condition. The OH^- groups absorbed on Ni ($Ni–OH_{ads}$) and Fe ($Fe–OH_{ads}$) sites and mainly on Ni sites are due to high oxidation and electron transfer between Ni and Fe. The bonded OH^- groups on the adjacent metal sites coupled through hydrogen bonding and exchange protons, which transferred to energetically favor Ni–O–Fe species. This can further transfer to Ni–O–O–Fe intermediate by breakdown Ni–O–Fe species. The O–O bonds are possibly attached to Ni (Ni–OO) sites due to the high oxidation of Ni and Fe, which enhance oxidation of Ni sites. The Ni–OOH species absorbed another OH^- species and release the oxygen molecules. The carbon provides a conductive channel for composite catalysts and also effectively protects the Ni_3S_2@FeNi-$NiFe_2O_4$ catalyst from agglomerating and dropping out from the microsphere.

The electrochemical impedance spectroscopy (EIS) test was conducted to investigate the OER kinetics at the electrode/electrolyte interface in 1 M KOH solution. The Nyquist plots are shown in Fig. 6b, which is fitted with an equivalent circuit (inset of Fig. 6b) and reveals the charge-transfer resistance (R_{ct}) of as-prepared samples. The R_{ct} values of the NiFe-$NiFe_2O_4$@Ni_3S_2/C-1, NiFe-$NiFe_2O_4$@Ni_3S_2/C-2, NiFe-$NiFe_2O_4$@Ni_3S_2/C-3, NiFe-$NiFe_2O_4$@Ni_3S_2/C-4, NiFe-$NiFe_2O_4$@Ni_3S_2/C-5, NiFe-$NiFe_2O_4$@Ni_3S_2/C-6, Ni-NiO/C-7, and Fe_3O_4/C-8 catalysts are 138.8, 74.28, 23.4, 27.6, 170.2, 219.1, 875.6, and 1674 Ω, respectively. The NiFe-$NiFe_2O_4$@Ni_3S_2/C-3 sample shows the lowest R_{ct} value due to the high metallic nature of Ni_3S_2 and high conductive carbon.

After the outstanding OER activity of Ni_3S_2@FeNi-$NiFe_2O_4$/C-3 sample, its stability was also studied. The stability of the composite catalyst was confirmed from both the CV cycling and the i-t test. The LSV curves are measured for fresh and after 1500 CV cycles, are shown in Fig. 6c. The sample shows almost similar LSV compared to the fresh one, and negligible decay of OER

performance after 1500 CV cycles, which indicates high stability of our catalyst. The Ni_3S_2@FeNi-$NiFe_2O_4$/C-3 composite sample was characterized by XRD, SEM, TEM, and XPS after 1500 CV cycles. XRD patterns (Fig. S9) show that the main diffraction peaks of fresh and used Ni_3S_2@FeNi-$NiFe_2O_4$/C-3 composite are consistent and display good stability. The SEM images still show a microsphere-like structure with some surface modification (Fig. S10a,b). The TEM image further revealed microsphere-like morphology (Fig. S10c) and rectangular flaky structures can be clearly observed, which are embedded in carbon (Fig. S10d). The survey XPS spectrum of shows peaks for Ni, Fe, S, C, N, and O (Fig. S11a). The Ni 2p region shows peaks for Ni $2p_{3/2}$ (873.85 eV) and Ni $2p_{3/2}$ (856.10 eV) of Ni^{2+} and two satellite peaks (Fig. S11b). The slightly shifting to the high binding energy of Ni^{2+} suggests further oxidation of Ni. The obvious change in Fe 2p peaks also indicates oxidation of Fe during the OER process (Fig. S11c). The peaks of the binding energy of S $2p_{3/2}$ (162.3 cV)

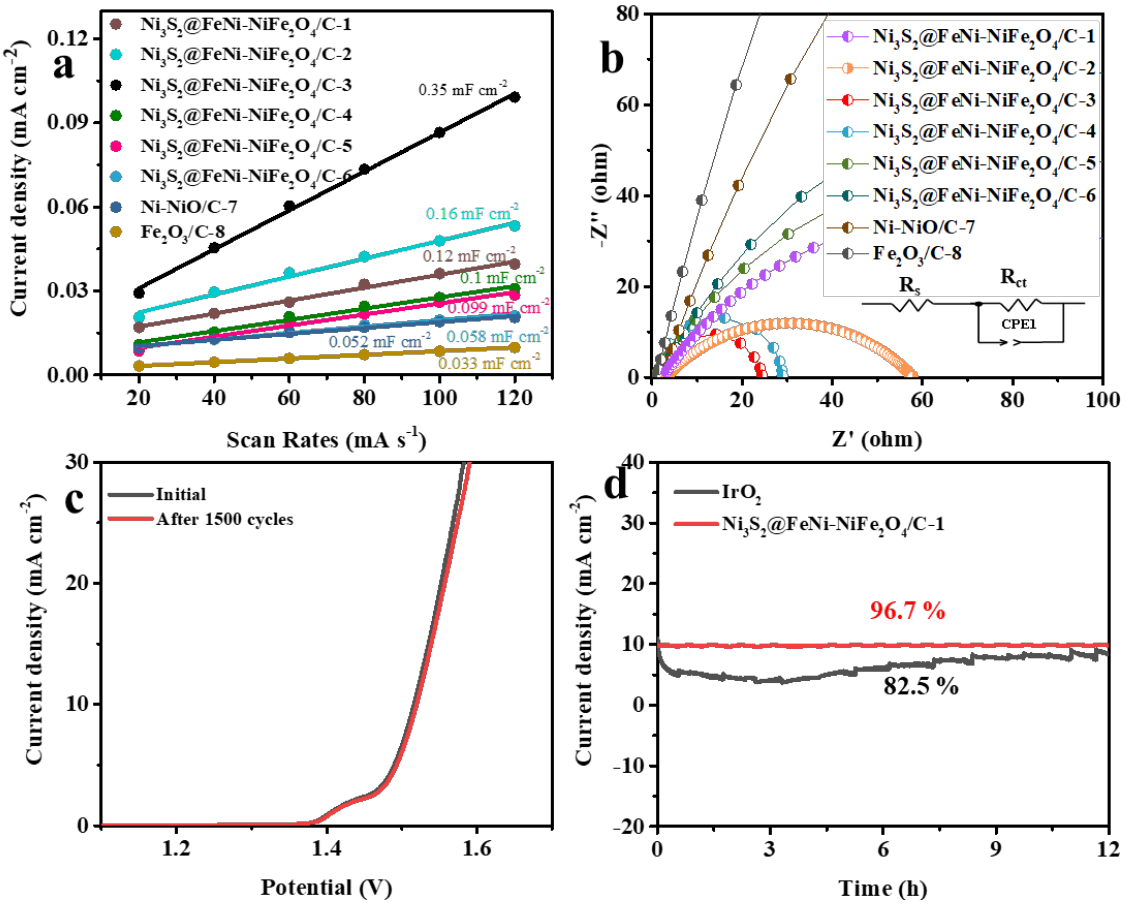

Fig. 6. (a) Calculated C_{dl} values. (b) Nyquist plots of as-prepared electrocatalysts and inset show the equivalent circuit used to fit the experimental data. (c) LSV curves of Ni_3S_2@FeNi-$NiFe_2O_4$/C-3 sample at the initial and after 1500 CV cycles. (d) Amperometric tests curve of Ni_3S_2@FeNi-$NiFe_2O_4$/C-3 and IrO_2 catalysts.

and S $2p_{1/2}$ (163.6 eV) in XPS spectrum of S 2p region became very weak, while peak intensity for sulphate species is much higher (Fig. S11d). This also suggests that the surface of S^{2-} is mostly converted to SO^{2-}_4 ions. No obvious changes are observed in C 1s (Fig. S11e) and N 1s spectra (Fig. S11f). It means that most N-doped carbons are inactive during the OER process. Furthermore, the i-t test of the Ni_3S_2@FeNi-$NiFe_2O_4$/C-3 and IrO_2 catalysts are investigated for long-term stability Fig. 6d. The difference in current density between initial and after 12 h of continuous

operation is only 0.3 and maintained 96.7 % of the current density, while IrO_2 losses current density of about 17.5 %, confirming the high stability of our product. The long-term stability of our composite can also be associated with N-doped carbon which effectively protects the Ni_3S_2@FeNi-$NiFe_2O_4$/C-3 from agglomerating.

4. Conclusion

In conclusion, a simple and low-cost heat-treatment method has been developed to synthesize the Ni_3S_2@FeNi-$NiFe_2O_4$/C-3 microspheres. Among the as-prepared samples, Ni_3S_2@FeNi-$NiFe_2O_4$/C-3 catalyst displays excellent OER performance with an overpotential of 280 mV at 10 mA cm^{-2} current density, small Tafel slope of 33.9 mV dec^{-1}, and good stability. It is believed that the enhanced electrocatalytic OER performance was due to the synergistic effect of heterointerfaces between Ni_3S_2 nanostrips and FeNi-$NiFe_2O_4$ nanoparticles. Therefore, Ni_3S_2@FeNi-$NiFe_2O_4$/C composites materials will be a promising and precious metal-free catalyst for OER.

Acknowledgments

This work is financially supported by the start-up foundation for the introduction of talent at Jiangsu University of Science and Technology, China.

References

[1] R. Boppella, J. W. Tan, J. W. Yun, S. V. Manorama, J. Moon. Coord. Chem. Rev. 427 (2021) 44.

[2] Y. Jiao, Y. Zheng, M. Jaroniec, S. Z. Qiao. Chem. Soc. Rev. 44 (2015) 2060-86.

[3] A. Wang, C. Zhao, M. Yu, W. Wang. Appl. Catal. B: Environ. 281 (2021)119514.

[4] K. Chen, S. Kim, R. Rajendiran, K. Prabakar, G. Li, Z. Shi, C. Jeong, J. Kang, O. L. Li. J. Colloid Interface Sci. 582 (2021) 977-990.

[5] X. Han, X. Li, J. White, C. Zhong, Y. Deng, W. Hu, T. Ma. 8 (2018) 1801396.

[6] J. Yu, B. Q. Li, C. X. Zhao, Q. Zhang. Energy Environ Sci. 13 (2020) 3253-3268.

[7] J. Chen, H. Chen, T. Yu, R. Li, Y. Wang, Z. Shao, S. Song. Electro. Ener. Rev. 4 (2021) 566-600.

[8] Z. P. Wu, X. F. Lu, S. Q. Zang, X. W. Lou. Adv. Funct. Mater. 30 (2020) 1910274.

[9] Y. Chen, H. Yao, F. Kong, H. Tian, G. Meng, S. Wang, X. Mao, X. Cui, X. Hou, J. Shi. V_2C Appl. Catal. B: Environ. 297 (2021) 120474.

[10] Y. P. Zhu, C. Guo, Y. Zheng, S. Z. Qiao. Acc. Chem. Res. 50 (2017) 915-923.

[11] Z. Shen, M. Qu, J. Shi, F.E. Oropeza, V.A. de la Peña O'Shea, G. Gorni, C.M. Tian, J.P. Hofmann, J. Cheng, J. Li, K.H.L. Zhang. J. Energy Chem. 65 (2022) 637-645.

[12] H. Chen, X. Liang, Y. P. Liu, X. Ai, T. Asefa, X. X. Zou. Adv. Mater. 32 (2020) 2002435.

[13] G. Lei, J. Ma, M. Zhao, S. Wu, H. He, H. Qi, W. Peng, X. Fan, G. Zhang, F. Zhang, Y. Li. J. Colloid Interface Sci. 602 (2021) 274-281.

[14] S. Govindaraju, S. K. Arumugasamy, G. Chellasamy, K. Yun. J. Hazard Mater. 421 (2022) 126720.

[15] T. X. Nguyen, Y. H. Su, C. C. Lin, J. M. Ting. Adv. Funct. Mater. 11, 2106229. https://doi.org/10.1002/adfm.202106229

[16] C. Song, S. Wu, X. Shen, X. Miao, Z. Ji, A. Yuan, K. Xu, M. Liu, X. Xie, L. Kong, G. Zhu, S. A. Shah. J. Colloid Interface Sci. 524, (2018) 93-101.

[17] Y. Li, G. Chen, Y. P. Zhu, Z. W. Hu, T. S. Chan, S. X. She, J. Dai, W. Zhou, Z. P. Shao. Adv. Funct. Mater. 31 (2021) 2103569.

[18] H. M. Fruehwald, R. B. Moghaddam, P. D. Melino, Ebralidze, II, O. V. Zenkina, E. B. Easton. Catal. Sci. Technol. 11 (2021) 4026-4033.

[19] J. Zhao, J. J. Zhang, Z. Y. Li, X. H. Bu. Small. 16 (2020) 2003916.

[20] Q. Kang, D. Lai, W. Tang, Q. Lu, F. Gao. Chem. Sci. 12 (2021) 3818-3835.

[21] X. An, D. Shin, J.D. Ocon, J.K. Lee, Y.I. Son, J. Lee, Chin. J. Catal. 35 (2014) 891-895.

[22] Y. J. Liu, X. L. Xie, G. X. Zhu, Y. Mao, Y. A. Yu, S. X. Ju, X. P. Shen, H. Pang. S J. Mater. Chem. A. 7 (2019) 15851-15861.

[23] Q. Xiang, F. Li, W. Chen, Y. Ma, Y. Wu, X. Gu, Y. Qin, P. Tao, C. Song, W. Shang, H. Zhu, T. Deng, J. Wu. ACS Energy Lett. 3 (2018) 2357-2365.

[24] S. A. Shah, X. Shen, A. Yuan, Z. Ji, X. Yue, G. Zhu, H. Zhou, K. Xu, J. Zhu, Y. Chen. Appl. Surf. Sci. 527 (2020) 146918.

[25] S. Liang, M. Jing, E. Pervaiz, H. Guo, T. Thomas, W. Song, J. Xu, A. Saad, J. Wang, H. Shen, J. Liu, M. Yang. ACS Appl. Mater. Interfaces 12 (2020) 41464-41470.

[26] S. A. Shah, G. Zhu, A. Yuan, N. Ullah, X. Shen, H. Khan, K. Xu, X. Wang, X. Yan. Dalton Trans. 49 (2020)15682-15692.

[27] C. Feng, M. B. Faheem, J. Fu, Y. Q. Xiao, C. L. Li, Y. B. Li. ACS Catal. 10 (2020) 4019-4047.

[28] J. M. P. Martirez, E. A. Carter. J. Am. Chem. Soc.141 (2019) 693-705.

[29] K. Wan, J. Luo, X. Zhang, P. Subramanian, J. Fransaer. J. Energy Chem. 62 (2021) 198-203.

[30] C. X. Zhao, B. Q. Li, M. Zhao, J. N. Liu, L. D. Zhao, X. Chen, Q. Zhang. Energy Environ. Sci. 13 (2020) 1711-1716.

[31] H. S. Ahn, A. J. Bard. J. Am. Chem. Soc. 138 (2016) 313-318.

[32] M. Gorlin, P. Chernev, J. F. de Araujo, T. Reier, S. Dresp, B. Paul, R. Krahnert, H. Dau, P. Strasser. J. Am. Chem. Soc. 138 (2016) 5603-5614.

[33] V. Vij, S. Sultan, A. M. Harzandi, A. Meena, J. N. Tiwari, W. G. Lee, T. Yoon, K. S. Kim. ACS Catal. 7 (2017) 7196-7225.

[34] N. T. Suen, S. F. Hung, Q. Quan, N. Zhang, Y. J. Xu, H. M. Chen. Chem. Soc. Rev. 46 (2017) 337-365.

[35] B. Q. Li, S. Y. Zhang, C. Tang, X. Y. Cui, Q. Zhang. Small. 13 (2017) 1700610.

[36] Y. Q. Yang, K. Zhang, H. L. Ling, X. Li, H. C. Chan, L. C. Yang, Q. S. Gao. ACS Catal. 7 (2017) 2357-2366.

[37] L. Y. Wang, Y. B. Li, Q. Q. Sun, Q. Qiang, Y. Q. Shen, Y. Ma, Z. L. Wang, C. Zhao. ChemCatChem. 11 (2019) 2011-2016.

[38] T. A. Ho, C. Bae, H. Nam, E. Kim, S. Y. Lee, J. H. Park, H. Shin. ACS Appl. Mater. Interfaces 10 (2018) 12807-12815.

[39] D. Lim, E. Oh, C. Lim, S. E. Shim, S.-H. Baeck. Electrochimi. Acta. 361 (2020) 137080.

[40] B. L. Li, Z. S. Li, Q. Pang, J. Z. Zhang. Chem. Eng. J. 401 (2020) 126045.

[41] Z. Cui, Y. C. Ge, H. Chu, R. Baines, P. Dong, J. H. Tang, Y. Yang, P. M. Ajayan, M. X. Ye, J. F. Shen. J. Mater. Chem. A. 5 (2017) 1595-1602.

[42] Y. Y. Wu, G. D. Li, Y. P. Liu, L. Yang, X. R. Lian, T. Asefa, X. X. Zou. Adv. Funct. Mater. 26 (2016) 4839-4847.

[43] N. Xu, Y. Zhang, T. Zhang, Y. Liu, J. Qiao. Nano Energy. 57, (2019) 176-185.

[44] H. Yang, Y. Liu, S. Luo, Z. Zhao, X. Wang, Y. Luo, Z. Wang, J. Jin, J. Ma. ACS Catal. 7 (2017) 5557-5567.

[45] J. Choi, D. Kim, W. Zheng, B. Yan, Y. Li, L. Y. S. Lee, Y. Piao. Appl. Catal. B: Environ. 286,

(2021) 119857.

[46] S. A. Shah, Z. Ji, X. Shen, X. Yue, G. Zhu, K. Xu, A. Yuan, N. Ullah, J. Zhu, P. Song, X. Li. ACS App. Energy Mater. 2 (2019) 4075-4083.

[47] H. Qian, B. Wu, Z. Nie, T. Liu, P. Liu, H. He, J. Wu, Z. Chen, S. Chen. Chem. Eng. J. 420, (2021) 127646.

[48] G. Zhu, X. Xie, Y. Liu, X. Li, K. Xu, X. Shen, Y. Yao, S. A. Shah. Appl. Surf. Sci. 442 (2018) 256-263.

[49] B. Zhang, L. Wang, Z. Cao, S. M. Kozlov, F. P. G. de Arquer, C. T. Dinh, J. Li, Z. Y. Wang, X. L. Zheng, L. S. Zhang, Y. Z. Wen, O. Voznyy, R. Comin, P. De Luna, T. Regier, W. L. Bi, E. E. Alp, C. W. Pao, L. R. Zheng, Y. F. Hu, Y. J. Ji, Y. Y. Li, Y. Zhang, L. Cavallo, H. S. Peng, E. H. Sargent. Nat. Catal. 3 (2020) 985-992.

[50] J. Liu, D. Zhu, T. Ling, A. Vasileff, S.-Z. Qiao. Nano Energy. 40 (2017) 264-273.

[51] Z. Liu, B. Tang, X. Gu, H. Liu, L. Feng. Chem. Eng. J. 395 (2020) 125170.

[52] S. A. Shah, X. Shen, M. Xie, G. Zhu, Z. Ji, H. Zhou, K. Xu, X. Yue, A. Yuan, J. Zhu, Y. Chen. Small. 15 (2019) 1804545.

[53] S. Ali Shah, L. Xu, R. Sayyar, T. Bian, Z. Liu, A. Yuan, X. Shen, I. Khan, A. Ali Tahir, H. Ullah. Chem. Eng. J. 428 (2022) 132126.

[54] Y. Lin, G. Chen, H. Wan, F. Chen, X. Liu, R. Ma. Small. 15 (2019) 1900348.

[55] K. Zhang, X. Min, T. Zhang, M. Si, J. Jiang, L. Chai, Y. Shi. ACS. Appl. Mater. Interfaces. 12 (2020) 54553-54562.

[56] M. Al-Mamun, H. Yin, P. Liu, X. Su, H. Zhang, H. Yang, D. Wang, Z. Tang, Y. Wang, H. Zhao. Nano Res. 10 (2017) 3522-3533.

[57] W. Liu, D. Rao, J. Bao, L. Xu, Y. Lei, H. Li. J. Energy Chem. 57 (2021) 428-435.

[58] Y. Wang, G. Qian, Q. Xu, H. Zhang, F. Shen, L. Luo, S. Yin. Appl. Catal. B: Environ. 286 (2021) 119881.

[59] C. Zhang, M. Antonietti, T. P. Fellinger. Adv. Funct. Mater. 24 (2014) 7655-7665.

[60] A. Indra, P. W. Menezes, N. R. Sahraie, A. Bergmann, C. Das, M. Tallarida, D. Schmeisser, P. Strasser, M. Driess. J. Am. Chem. Soc. 136 (2014) 17530-17536.

[61] Y. Wang, W. Ding, S. G. Chen, Y. Nie, K. Xiong, Z. D. Wei. Chem. Commun. 50 (2014) 15529-15532.

[62] L. Du, L. L. Luo, Z. X. Feng, M. Engelhard, X. H. Xie, B. H. Han, J. M. Sun, J. H. Zhang, G. P. Yin, C. M. Wang, Y. Wang, Y. Y. Shao. Nano Energy. 39 (2017) 245-252.

[63] V. Vij, S. Sultan, A. M. Harzandi, A. Meena, J. N. Tiwari, W. G. Lee, T. Yoon. K. S. Kim. ACS Catal. 7 (2017) 7196–7225.

[64] F. Song, M. M. Busch, B. Lassalle-Kaiser, C. S. Hsu, E. Petkucheva, M. Bensimon, H. M. Chen, C. Corminboeuf. X. Hu. ACS Cent. Sci. 5(3) 558–568 (2019).

[65] M. Busch. Curr. Opin. Electrochem. 9 (2018) 278-284.

[66] B. Zhang, X. L. Zheng, O. Voznyy, R. Comin, M. Bajdich, M. Garcia-Melchor, L. L. Han, J. X. Xu, M. Liu, L. R. Zheng, F. P. G. de Arquer, C. T. Dinh, F. J. Fan, M. J. Yuan, E. Yassitepe, N. Chen, T. Regier, P. F. Liu, Y. H. Li, P. De Luna, A. Janmohamed, H. L. L. Xin, H. G. Yang, A. Vojvodic, E. H. Sargent. Science. 352 (2016) 333-337.

[67] D. K. Bediako, Y. Surendranath, D. G. Nocera. J. Am. Chem. Soc. 135 (2013) 3662-3674.

[68] G. X. Zhu, X. L. Xie, X. Y. Li, Y. J. Liu, X. P. Shen, K. Q. Xu, S. W. Chen. ACS. Appl. Mater. Interfaces. 10 (2018) 19258-19270.